Composites Part C: Open Access 18 (2025) 100632

Contents lists available at ScienceDirect

Composites Part C: Open Access

journal homepage: www.sciencedirect.com/journal/composites-part-c-open-access

Combining hydromorphic and shape-shifting effects for programmable passive actuation in 4D-printed biocomposites

Phil Aron Bachmann [a,b], Kim Pickering [b], Christian Gauss [b,*]

[a] City University of Applied Sciences Bremen, Bremen 28199, Germany
[b] School of Engineering, The University of Waikato, Hamilton 3216, New Zealand

ARTICLE INFO

Keywords:
Hydromorphism
Shape-shifting
Actuator
Biocomposite

ABSTRACT

4D printing involves the fabrication of structures that respond dynamically to external stimuli. While various actuation mechanisms have been extensively studied, the integration of multiple actuation effects remains relatively unexplored. This study examines the combined influence of hydromorphic and shape-shifting effects in a biocomposite containing 40 wt% cellulose fibres. The biocomposite was combined with polylactide (PLA) and processed via 3D printing to produce bi-material strips, which were then comprehensively analysed for their material properties and shape-changing behaviour. Upon immersion in water, the biocomposite expanded by 3.2 % perpendicular to the printing direction and exhibited a marked decrease in Young's modulus with increasing water content. Bi-material strips 1 mm thick displayed pronounced hydromorphic behaviour, achieving maximum curvatures of 0.036 - 0.052 mm^{-1} depending on the passive-to-active layer thickness ratio. Thicker strips (4 mm) reached 0.012 mm^{-1} under the same conditions. When both heat and water were applied as external stimuli, the biocomposite and neat PLA layers became simultaneously active, and curvatures of up to 0.057 mm^{-1} were obtained for 4 mm strips. This curvature surpassed the hydromorphic-only and shape-shifting-only responses by factors of 4.77 and 1.82, respectively. The results demonstrate that integrating water- and heat-induced stimuli increases achievable curvature and accelerates the response, enabling high-curvature deformations even in relatively thick structures. The approach therefore holds promise for applications that demand significant shape transformations without compromising structural integrity.

1. Introduction

Composites produced from the reinforcement of bio-derived thermoplastics such as polylactide (PLA) with lignocellulosic fibres have attracted significant interest due to their cost-effectiveness, environmental benefits, improved end-of-life management, and enhanced mechanical properties. A frequently cited drawback of these composites is the hydrophilic behaviour of lignocellulosic fibres, which causes anisotropic swelling in the transverse direction when exposed to moisture [1,2]. Swelling and water absorption can affect the composite's mechanical properties [2]. Paradoxically, natural systems such as pinecones exploit this phenomenon for functional purposes. Their scales utilize a bilayer architecture of lignocellulosic tissues with differential coefficients of moisture expansion (CMEs), enabling humidity-driven passive actuation to release seeds—a mechanism akin to the thermal bending of bimetallic strips but governed by hygroscopic gradients rather than temperature [3].

Additive manufacturing (AM) has unlocked novel pathways to replicate such bioinspired hygromorphic structures. By 3D printing cellulose-based/natural fibre-reinforced composites, it is possible to engineer moisture-responsive actuators that mimic biological systems [4–7]. Lyocell fibres, a type of regenerated cellulose produced by dissolving and regenerating cellulose into continuous fibres using N-methylmorpholine-N-oxide (NMMO) [8], are particularly advantageous due to their uniform dimensions and predictable properties. These characteristics enhance processability [9] and facilitate the 3D printing of biocomposites [10]. Additionally, lyocell fibres exhibit excellent mechanical properties [8] and hygroscopic behaviour [11]. Extrusion-based 3D printing techniques such as fused deposition modelling (FDM), allows the printing of filament layers to create complex geometries [12]. The high shear stresses experienced in the nozzle during printing partially align the natural/cellulose fibres in the biocomposite with the deposition path's raster angle [10]. Cellulose fibres (and natural fibres) have preferential swelling in the transverse direction

* Corresponding author.
E-mail address: cgauss@waikato.ac.nz (C. Gauss).

https://doi.org/10.1016/j.jcomc.2025.100632

Available online 5 August 2025

[7] and with a predominant fibre orientation induced by printing in the biocomposites, a high coefficient of moisture expansion can be achieved in a direction perpendicular to the printing direction. When paired with a PLA passive layer with a negligible coefficient of moisture expansion, this bilayer configuration creates a hygromorphic structure that bends in response to changes in moisture content, with bending kinetics quantifiable via modified Timoshenko bimetallic strip models [4,5,13].

When 3D printing is used to create structures that alter their geometry when exposed to specific external conditions, it is referred to as 4D printing [14]. Various forms of 4D printing use different stimuli to trigger actuation, including heat [15], UV radiation [16], moisture [4], and pH [17]. Many of the studies on thermally induced shape change rely on the shape-memory effect of polymers [15,16], which is also inherent to PLA. Heating PLA to its glass transition temperature (T_g) increases the mobility of its polymer chains in the amorphous regions, enabling mechanical deformation into a state of lower entropy. Rapid cooling immobilises the chains, locking them into this temporary and metastable state. Upon reheating above the T_g, the chains revert to their high-entropy (lowest energy), randomly coiled conformation, recovering their original and permanent shape [18,19]. The shape-shifting behaviour of PLA follows a similar mechanism to the shape-memory effect. During 3D printing, shear stresses and cooling stretch and constrain the polymer chains, storing strain within them. This state is analogous to the temporary shape of the shape-memory effect. When reheated, this stored strain is released, causing irreversible shrinkage in PLA [15]. By adjusting printing speed and cooling rates, different strain levels can be introduced between layers, leading to differential shrinkage upon heating and enabling controlled bending [20].

While many studies have explored different stimuli induced actuation, few have investigated their combination. In this work, we bridge this gap by examining the integration of hydromorphic and shape shifting mechanisms to achieve greater shape transformation and faster response. Bilayer strips were printed comprising a PLA composite made with 40 wt % of lyocell fibres and a passive PLA layer to create hydromorphic structures. These structures were systematically characterized under different water content and thermal stimuli to quantify bending magnitude, actuation kinetics, and the interplay between hydroscopic swelling and stress-driven recovery. Our approach leverages the complementary strengths of water/moisture responsiveness and thermally amplified shape-shifting, offering a pathway to enhance the speed and programmability of 4D-printed actuators.

2. Materials and methods

For the 4D-printing, a biocomposite was produced with a content of 40 wt % lyocell fibres (FCP300, with a nominal length of 300 μm and a linear density of 1.3 dtex, sourced from Lenzig®, Austria) and 60 wt % polylactide (PLA) grade 2003D, NatureWorks® (Plymouth, MN, USA), which has a melt flow index (MFI) of 6 g/10 min at 210 °C under 2.16 kg and a specific gravity of 1.24 g/cm^3.

2.1. Production of the composite

Firstly, the moisture content of the lyocell fibres was determined through an infra-red moisture analyser. Based on the moisture content, 300 *g* of dry fibre equivalent was soaked for 24 h in tap water, with a ratio of 10 g/L. Subsequently, the fibres were mechanically fibrillated with a Masuko Sangyo supermasscolloider (MKZA10–15JIV, Kawaguchi, Japan). Increased roughness and surface fibrillation of lyocell fibres improves the adhesion of the PLA matrix and the fibres, therefore enhancing the composite's mechanical properties [21,22]. The fibres were processed at 1500 rpm and the grinding disk distance was decreased from 200 μm, to 100 μm, to 50 μm, and close to 0 μm until the desired fibrillation was achieved. After each pass, samples were analysed with an Olympus BX53 microscope (Olympus, Tokyo, Japan) to verify the level of fibrillation. Additional scanning electron microscopy images of the fibres before and after fibrillation are available in the supplementary file (Figure S1). After the fibrillation, the lyocell fibres were centrifuged and stored in a refrigerator at 4 °C for further processing. In the next step, the lyocell fibres were coated with a Landy PL-3000 PLA emulsion (40 mass % of solid content, Miyoshi Oil and Fat Co., Ltd, Tokyo, Japan). The emulsion was added to the fibres in a 10 mass % relation and mixed through a LabTech LMX10-VS high shear mixer (Labtech Engineering Company, Ltd., Samut Prakan, Thailand) for 10 min at 3000 rpm. Lastly, the PLA-coated lyocell fibres were dried at 45 °C for 24 h. The day prior to the compounding, the lyocell fibres were dried at 45 °C for 6 h and then at 103 °C overnight. On the day of the compounding, the lyocell fibres and PLA2003D were both vacuum-dried at 80 °C in a Thermoscientific VT 6060 M-BL (Thermo Fisher Scientific Inc., Waltham, MA, USA) for 4 h. Afterwards, the materials were manually fed to a twin-screw extruder (Process 16 Parallel Twin-Screw Extruder, Thermo Fisher Scientific Inc.,Waltham, MA, USA) and processed with a temperature profile of 165 °C, 180 °C, and the rest 185 °C at 70 rpm. Subsequently, the composite was granulated into pellets under 4 mm, dried at 103 °C for 1 hour, and added to the main feeder of the twin-screw extruder for a second processing. The production of the biocomposite was completed with another granulation.

2.2. Production of the filament

The biocomposite pellets were fed to a single screw extruder (EX2, Filabot. Barre, VT, USA) at 180 °C to produce the 3D printing filament. The filament was air cooled (using a Filabot Airpath. Barre, VT, USA) and spooled with a spooling system. The rate of extruding, cooling, and spooling were adjusted to obtain a filament with diameter of 1.75 ± 0.05 mm.

2.3. 3D printing

All specimens were printed with Makergear™ M2 desktop 3D printer (Beachwood, OH, USA), using the software Simplify 3D®, version: 3.1.1 2016 (Cincinnati, OH, United States). A stainless-steel nozzle (diameter of 0.50 mm) was used, with a printing layer height of 0.1 mm and an infill percentage of 100 %. The printing speed was set constant at 2400 mm.min^{-1}, as well as the nozzle and bed temperatures (210 °C and 50 °C, respectively). Cooling was induced by a fan with the speed set on 50 %. Before 3D printing, the filament was vacuum-dried at 45 °C for 2 h. The biocomposites and neat PLA were printed using the same printing conditions.

2.4. Materials characterization

2.4.1. Differential scanning calorimetry - DSC

For the DSC analysis, filament samples of 5 - 10 mg were used. The samples were sealed in an aluminium crucible and analysed in a DSC3500 Sirius (NETZSCH GmbH & Co., Selb, Germany) between 20 - 200 °C at a heating rate of 10 °C.min^{-1} and nitrogen flow of 60 mL.min^{-1}. The data was analysed to determine the glass transition (T_g), melting (T_m) and cold crystallization (T_{cc}) temperatures. The degree of crystallinity (X_c) of the samples was calculated using Eq. (1):

$$X_c = \frac{(\Delta H_m - \Delta H_{cc})}{\Delta H_f \times X_{PLA}}.100 \quad (1)$$

where ΔH_m and ΔH_{cc} represent the enthalpies of melting and cold crystallization, respectively, ΔH_f corresponds to the melting enthalpy of fully crystalline PLA (93 J/g) [23], and X_{PLA} denotes the PLA weight fraction in the composite.

2.4.2. Dynamic mechanical analysis - DMA

Rectangular samples (75 × 7 × 1.5 mm^3) of the biocomposites and neat PLA were 3D printed with raster angles of 0° and 90° for DMA

analysis. The analysis was performed in a DMA8000 (Perkin Elmer, Waltham, MA, USA) using a single cantilever mode, at a frequency of 1 Hz, displacement of 0.05 mm, and using a heating rate of 2 °C.min^{-1} from 25 - 140 °C.

2.4.3. Expansion testing

The biocomposite was investigated on its water-induced expansion (hydroexpansion). For this, 5 rectangular specimens with 20 × 10 × 1.2 mm^3 were 3D printed using a raster angle of 90° The perimeter was removed from the slicing software, as it would have interfered with the expansion behaviour. To uniformly measure the hydroexpansion, the specimens were marked at 3 spots for each dimension. Before the experiments, the specimens were vacuum-dried for 4 h, weighed, and measured with a digital calliper. Afterward, the specimens were completely submerged in water at room temperature. The specimens dimensions and weight were tracked at different time points over 336 h. The water content at a given point in time was calculated with Eq. (2):

$$M_t(\%) = \frac{W_t - W_0}{W_0} \cdot 100 \quad (2)$$

where W_t is the weight at time t after contact with water and W_0 the dry weight (before immersion). Furthermore, the relative expansion was calculated using the Eq. (3):

$$\beta_t(\%) = \frac{I_t - I_0}{I_0} \cdot 100 \quad (3)$$

where I_t is the dimension at time t after exposure and I_0 the dry/initial dimension [5].

2.4.4. Tensile testing

The influence of water content on the tensile properties of the biocomposite was investigated through tensile testing. Modified ASTM D638 - type V dog bone specimens of 73.03 × 19.06 × 1.2 mm (L x W x H) with a 90° raster angle and without a perimeter were 3D-printed. Before tensile testing, the specimens were submerged in water for 2, 24, 48, and 72 h to achieve different moisture contents. A set of samples was also conditioned in room temperature and relative humidity for 168 h. Five samples per condition were tested. Before the water immersion, the specimens were vacuum dried at 45 °C for 2 h. Their weight was measured immediately after vacuum-drying, as well as after removing them from the water. The water content of the specimens was calculated with the Eq. (2). Tensile testing was conducted with an Instron 5982 mechanical testing machine (© Illinois Tool Works Inc., IL, USA) using a 5 kN load cell at a constant crosshead displacement of 2 mm.min^{-1}. A 10 mm clip-on extensometer was used to measure strain. A digital calliper was used to measure width and thickness of the samples before testing.

2.5. Shape-morphing behaviour

2.5.1. Printing bi-material strips

To assess the hydromorphic and shape-shifting effects, bi-material strips consisting of the 40 wt % lyocell biocomposite (L40) and PLA2003D were 3D printed. The biocomposite was used to print the active layers in a 90° raster angle, while neat PLA printed in a 0° raster angle was used for the passive layers (see Fig. 1). When printing the bi-material strips, the biocomposite was printed first, followed by neat PLA. The perimeter of the bi-material strips was removed from the slicing software. Moreover, different ratios of passive to active layers (m) were considered. These ratios were chosen based on the hypothesis that the Young's modulus of the biocomposite active layer decreases with increasing water content, thereby increasing the stiffness ratio (n). Consequently, configurations with m values below 1.0 were expected to exhibit higher curvature change coefficients, consistent with the findings of Holstov et al. (2015) [24].

All specimens had the same length of 80 mm with a width of 10 mm, while the total thickness was varied (see Table 1). In the samples used to assess the combined hydromorphic and shape-shifting affects, both layers printed with the biocomposite and neat PLA worked as active layers. In this case, the biocomposite printed at a 90° raster angle was activated by the increase in water content (hydro active layer) while the neat PLA layer printed a 0° raster angle was activated by the increase in temperature (thermo active layer). Additionally, mono-material strips consisting of neat PLA for both 90° and 0° layers were 3D-printed and used as reference for the combined approach tests (hydromorphic + shape-shifting). Each sample condition was named according to its material (M for mono-material and Bm for bi-material), total thickness (0.8 and 4.0 mm), and the ratio of active to passive layer (1.0, 0.6, and 0.33). The samples used for the combined effects include "C" in their names.

2.5.2. Testing of the hydromorphic behaviour

The hydromorphic capabilities of samples Bm/0.8–1 to Bm/0.8–0.3 (3 samples per condition), condition 1–3, were assessed (see Fig. 2). For this, the specimens were firstly vacuum-dried at 45 °C for 2 h. Afterward, the specimens were soaked in room-temperature water. Their dry weight (as-printed condition) and after 2, 24, 48, 72, and 168 h of immersion was measured with a semi-analytical scale to calculate the water content. Furthermore, to later calculate the curvatures, photos of the specimens were taken for each time step. Additionally, the curvatures were tested on their reversibility. For this, the specimens were placed on a bench at room temperature and humidity for 48 h and then

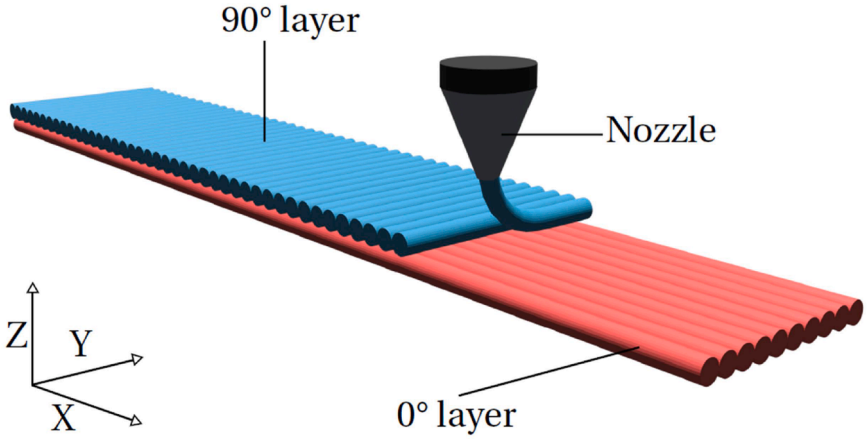

Fig. 1. . Representation of the 3D printed samples used to assess shape-morphing behaviour. For the bi-material strip, the biocomposite was printed in a 90° raster angle (blue), and the neat PLA in a 0° raster angle. For the mono-material strips, both layers were printed with neat PLA.

Table 1
Overview of the different conditions of bi-material (Bm) and mono-material (M) strips used for the tests to assess hydromorphic only behaviour and combined hydromorphic + shape-shifting behaviour. The conditions differ in their thickness (t), their raster angle (RA), and the material of their active and passive layers (or t_1 and t_2 in the case of the combined samples). Furthermore, depending on the condition, the total thickness (T) and the ratio of active to passive layer (m) may differ.

Condition	Sample type ID	Active layer			Passive layer			Total	Ratio
		t_a (mm)	RA (deg)	Material	t_p (mm)	RA (deg)	Material	T (mm)	$m = \frac{t_p}{t_a}$
	Hydromorphic								
1	Bm/0.8–1	0.4	90	L40	0.4	0	PLA	0.8	1.00
2	Bm/0.8–0.6	0.5	90	L40	0.3	0	PLA	0.8	0.60
3	Bm/0.8–0.3	0.6	90	L40	0.2	0	PLA	0.8	0.33
4	Bm/4–1	2.0	90	L40	2.0	0	PLA	4.0	1.00
	Hydromorphic + Shape-shifting								
		Hydro active layer			Thermo active layer			Total	Ratio
		t_1 (mm)	RA (deg)	Material	t_2 (mm)	RA (deg)	Material	T (mm)	$m = \frac{t_2}{t_1}$
5	C-Bm/4–1	2.0	90	L40	2.0	0	PLA	4.0	1.00
6	C-Bm/4–0.6	2.5	90	L40	1.5	0	PLA	4.0	0.60
7	C-Bm/4–0.3	3.0	90	L40	1.0	0	PLA	4.0	0.33
5r	C-M/4–1	2.0	90	PLA*	2.0	0	PLA	4.0	1.00
6r	C-M/4–0.6	2.5	90	PLA*	1.5	0	PLA	4.0	0.60
7r	C-M/4–0.3	3.0	90	PLA*	1.0	0	PLA	4.0	0.33

* The PLA in these layers of the mono-material samples work as passive layers.

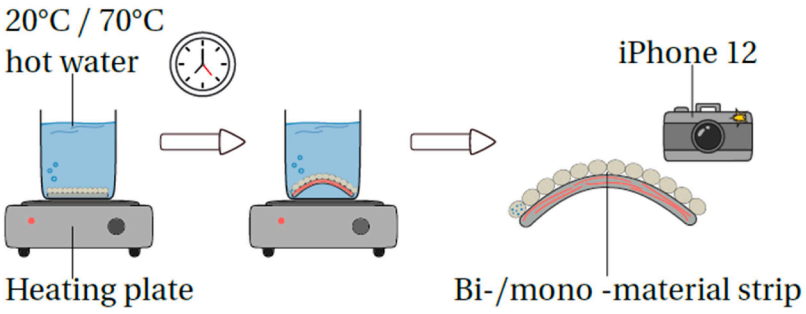

Fig. 2. Experimental setup to test the shape-morphing behaviour. For the characterization of the hydromorphic capabilities, bi-material strips were immersed in water at 20 °C. Mono-material and bi-materials strips were investigated on their shape-morphing behaviour in water at 70 °C water.

dried in a vacuum oven for 4 h at 45 °C. After 2, 24, and 48 h, and after the 4 h of vacuum-drying, their weight was measured, and a picture was taken. The thicker bi-material strip (Bm/4–1) was immersed in water at room temperature for 168 h and compared with the other samples used to evaluate the combined hydromorphic and shape-shifting effects.

2.5.3. Assessment of the combination of hydromorphic and shape-shifting effects

The combination of the hydromorphic and shape-shifting effects of samples C-Bm/4–1 to C-Bm/4–0.3 (3 samples per condition), conditions 5–7, was evaluated (see Fig. 2). Prior to testing, the specimens were dried in a vacuum oven for 2 h at 45 °C and then submerged in 70 °C water for up to 24 h. Their weight was measured in their as-printed condition (dry) and after 30 min and 24 h of immersion. Additionally, the specimens were photographed to later determine their curvatures. The mono-material reference strips (PLA only) were tested under the same conditions (samples C-M/4–1 to C-M/4–0.3).

2.5.4. Analysis of the shape-morphing behaviour

The moisture content of the bi-material strips was calculated with Eq. (2). Furthermore, the curvature and the relative expansion of the layers of the bi-material strips were determined through ImageJ® (Wayne Rasband, Version 1.54d National Institutes of Health, USA) as shown in Fig. 3 using Eqs. (3) and 4:

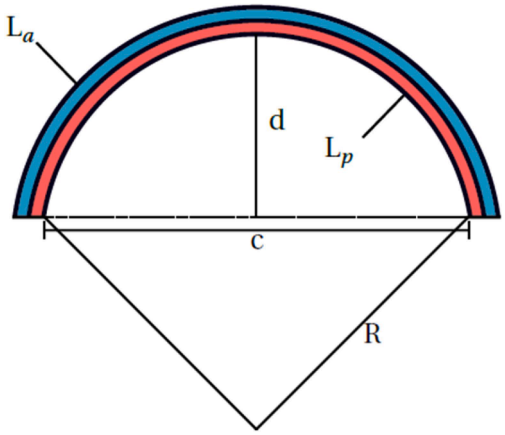

Fig. 3. The radius (R) of curvature and the length of the layers were determined. The height (d) and length (c) of the curvature, along with the lengths of the active and passive layers (L_a and L_p), were measured using ImageJ, as shown in the image.

$$\Delta K = \frac{1}{R} = \frac{8d}{c^2 + 4d^2} \tag{4}$$

where ΔK is the curvature, c is the length, d the height and R the radius of curvature.

2.5.6. Timoshenko model

The experimentally obtained curvatures of the hydromorphic behaviour were compared with the theoretical curvature values predicted by the modified Timoshenko equation (see Eq. (5)):

$$\Delta K = \frac{\Delta\beta\Delta C f(m,n)}{t} \tag{5}$$

where ΔK is the curvature, $\Delta\beta$ the difference in the coefficient of hydroscopic expansion between the active and passive layer, ΔC the water loss between dry and wet state, t the total thickness of the strip and f(m,n) a dimensionless coefficient that was calculated with Eq. (6) and 7:

$$f(m,n) = \frac{6(1+m)^2}{3(1+m)^2 + (1+mn)\left(m^2 + \frac{1}{mn}\right)} \tag{6}$$

$$m = \frac{t_p}{t_a} \text{ and } n = \frac{E_p}{E_a} \tag{7}$$

where m and n are the ratios of thicknesses (t) and Young's moduli (E) of the passive to the active layer, respectively [25]. Table 2 gives an overview of the values that have been used for the parameters in the modified Timoshenko equation.

2.6. Data analysis

Fitted curves for the raw data sets of tensile testing and the hygro-expansion were created in Matlab (Version R2023b, MathWorks®, Natick, USA) using the Curve Fitting Toolbox (version 23.2,MathWorks®, Natick, USA).

3. Results

3.1. Material characterization

Fig. 4 presents the differential scanning calorimetry (DSC) thermograms for neat PLA and the biocomposites (L40) filaments. Both the neat PLA and the biocomposites exhibit similar graphs, featuring three distinct peaks with varying intensities (see Table 4).

Table 3 summarises the obtained results. The glass transition temperature (T*g*) is slightly higher for the biocomposite with a difference of 2.6 °C. In contrast, the cold crystallization temperature (T*cc*) of the biocomposite is lower with a difference of 5.9 °C, while the cold crystallization heat (ΔH*cc*) is 216.8 % higher compared to neat PLA. Furthermore, the biocomposites melting heat (ΔH*m*) is increased by 37.9 %, while the melting temperature is roughly the same. Similar behaviour is observed in PLA composites reinforced with other natural fibres such as harakeke (New Zealand flax) and bleached soft wood pulp [26,27].

The log-scaled plots of the storage modulus, loss modulus, and tan δ in Fig. 5 emphasize the differences in mechanical and damping behaviour of the biocomposite and neat PLA with different raster angles. All raster angle combinations show 3 distinct regions. A plateau of the storage modulus between 30 - 50 °C, a rapid decrease of the storage modulus between 50 - 65 °C accompanied by a corresponding increase in tan δ, and a secondary rise in the storage modulus between 80 - 90 °C for the biocomposite and between 90 - 110 °C for the neat PLA. Among all samples, the 0° biocomposite exhibits the highest storage modulus across the entire temperature range, decreasing from 3.75 GPa at 30 °C to 0.20 GPa at 70 °C. In contrast, the 0° neat PLA shows lower values, ranging from 2.31 GPa at 30 °C to 0.035 GPa at 70 °C. The difference in storage modulus between the 90° PLA and 90° biocomposite is comparatively smaller. Specifically, the storage modulus of the 90° PLA is 0.12 GPa lower at 30 °C and 0.05 GPa lower at 70 °C than that of the corresponding biocomposite.

Comparable improvements have been reported for other short-fibre systems. Incarnato et al. recorded a 47 % storage modulus gain at 35 °C with 18 wt % microcrystalline cellulose (MCC) [28]. 3D-printed PLA composites reinforced with 30 wt % bleached harakeke fibres likewise showed a substantial rise in storage modulus—from 2.87 GPa for neat PLA to 5.48 GPa for the biocomposite at 25 °C; at 60 °C, the modulus of this biocomposite was roughly 5.5 times higher than that of neat PLA [29]. Espinach et al. reported room-temperature modulus gains of 1.3–1.7 times for PLA reinforced with 20–30 wt % bleached Kraft soft-wood fibres [27]. Similarly, the composites maintained higher storage modulus at temperatures above T_g.

With regard to tan δ, both PLA raster angles show higher peak values compared to the biocomposite. The 90° neat PLA has the highest peak, which is 116.2 % greater than that of the 0° biocomposite with the lowest tan δ peak. Notably, the biocomposite presents similar tan δ peak values for both raster angles, 0.713 and 0.843 for the 0° and 90° biocomposites, respectively. In comparison, the difference between tan δ peaks for the neat PLA raster angles is 3.17 times higher. Additionally, the biocomposite samples demonstrate a more substantial increase in storage modulus beyond 80 °C compared to the neat PLA, which may be attributed to crystallization occurring at elevated temperatures, as observed in other studies with short-fibre PLA composites [27,29].

The biocomposites consistently exhibit higher storage and loss moduli, indicating improved thermal-mechanical stability. Notably, the 0° biocomposite shows the highest loss modulus peak around 55–60 °C, suggesting enhanced energy dissipation likely due to the alignment of the reinforcing fibres along the loading direction. The broader and lower tan δ peaks in the biocomposites further reflect restricted chain mobility and a more gradual glass transition.

Fig. 6 illustrates the Young's modulus and tensile strength at different water contents of the biocomposite 3D printed using a raster angle of 90° (applied load perpendicular to printing direction). Additional results of tensile testing of the biocomposite printed at different raster angles are given in Table S1 (tested in standardized conditions, without influence of water content). Both tensile strength and Young's modulus of the biocomposite decreased linearly with increasing water content. The Young's modulus dropped by 69.2 %, from 3.20 GPa (dry condition) to 1.23 GPa, at an average water content of 14.3 %. Similarly, tensile strength decreased by 64.0 %, from 20.0 MPa to 10.1 MPa. The Young's modulus and water content exhibit a linear relationship, with a reasonably high coefficient of determination ($R^2 = 0.9419$).

The hydroexpansion behaviour of the biocomposite, perpendicular to the printing direction, is depicted in Fig. 7. It is noticeable that the hydroexpansion increases following a sigmoidal function (Gompertz model) with an increase in water content, with a R^2 of 0.9996. The highest increase in expansion, from 0.48 ± 0.1 % to 2.50 ± 0.1 %, occurs between water contents of 4.7 ± 1.2 % and 11.6 ± 0.3 %. At water contents close to 15 %, the expansion of the biocomposites started to stabilize achieving a maximum value of 3.17 ± 0.1 % at a water content of 21.5 ± 0.7 %.

Table 2
Overview of the parameters used in the Timoshenko equation. $\Delta\beta\Delta C$ and E_a were obtained through the hydroexpansion and tensile testing results (loading direction perpendicular to printing direction), respectively. Furthermore, a Young's Modulus of 3.3 GPa was used for the passive layer [4,22].

$\Delta\beta\Delta C$	E_a – Composite (GPa)	E_p – PLA (GPa)
Results hydroexpansion	Results tensile testing (wet state)	3.3

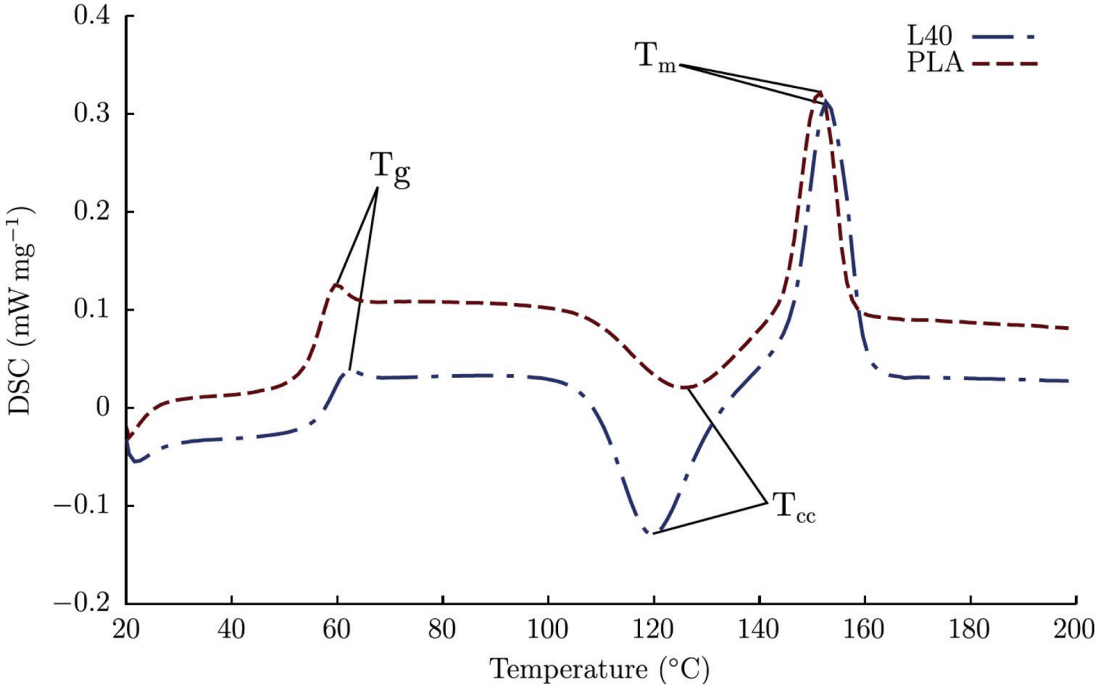

Fig. 4. Comparison between DSC thermograms of the 40 wt % lyocell biocomposite (L40) and neat PLA, where T_m is the melting temperature, T_{cc} is the cold crystallization temperature, and T_g is the glass transition temperature.

Table 3
Summary of the DSC results including the glass transition temperature (T*g*), the temperature (T*cc*) and heat (ΔH*cc*) of cold crystallization, the temperature (T*m*) and heat (ΔH*m*) of melting, and the degree of crystallinity (X*c*) of neat PLA and the 40 wt % lyocell biocomposites (L40).

Sample	T_g (°C)	T_{cc} (°C)	ΔH_{cc} (J/g)	ΔH_m (J/g)	T_m (°C)	X_c (%)
Neat PLA	59.9	125.6	−4.644	11.28	151.3	7.16
L40	62.5	119.7	−14.71	15.56	152.8	1.51

3.2. Hydromorphic behaviour

Fig. 8 shows the moisture-induced curvature of the biomaterial strips with total thickness of 0.8 mm, conditions 1 – 3 (see Table 1). Evidently, with an increase in the water content, the curvature increases. After 2 h of immersion, condition 1 (samples Bm/0.8–1 with $\frac{t_p}{t_a} = 1$) has the highest curvature (0.010 ± 0.002 mm^{-1}) which is 18.75 % higher than condition 3 (samples Bm/0.8–0.3 with $\frac{t_p}{t_a} = 0.33$) with the lowest curvature. With an increase of water content over time, however, this relation changes, and after 168 h, condition 3 achieves the overall maximum curvature of 0.0516 ± 0.0006 mm^{-1} with a water content of 13.03 ± 0.92 %, which is 42.2 % higher than that of condition 1 (curvature of 0.0363 ± 0.001). The highest increase in curvature and water content is between 2 - 24 h for all conditions. In this range, condition 3 has the highest increase of all conditions with 453.3 % in curvature and 94.43 % in moisture content. Regarding the reversibility of the moisture-induced curvature, condition 3 has the lowest reversibility, with 73.16 %, after 4 h of vacuum-drying (a reversibility of 100 % means that the sample, once fully dried, returns to its original flat state). Despite a moisture content of 0 % after 4 h of vacuum-drying, the curvatures of conditions 2 and 3, 0.0123 mm^{-1} and 0.0138 mm^{-1} respectively, remain higher than the curvature after 2 h of immersion in water. Solely, the curvature of condition 1 is 7.68 % lower than that after 2 h.

The experimental values obtained for hydromorphic curvatures are compared to the theoretically predicted curvatures of the modified Timoshenko model in Fig. 9. All the values used for the calculation of the predicted curvatures are given in the supplementary file (Table S2). It is visible that the predicted curvatures are lower for samples Bm/0.8–0.6 and Bm/0.8–0.3 compared to the experimental data for all water contents. Up to 48 h, it is the same situation for the sample with higher *m* value, Bm/0.8–1. However, after 48 h, the predicted curvatures exceed the experimental data. The average difference between the predicted and experimental curvatures is the lowest for Bm/0.8–1 with 19.34 % and the highest for Bm/0.8–0.3 with 26.2 %. Furthermore, the modified Timoshenko equation contradicts the experimental data by predicting Bm/0.8–0.6 to have the highest curvatures between 24 - 72 h. In contrast, the experimental data shows that it is Bm/0.8–0.3 that has the highest curvature for the water contents at those time steps.

3.3. Shape-shifting and combination of effects

Fig. 10 shows the curvature of the bi-material and their mono-material reference strips 0.5 h and 24 h after immersion in water at 70 °C. It is observable that the bi-material strips achieve higher curvature values for all conditions than their mono-material counterparts. The highest curvature value of 0.057 ± 0.001 mm^{-1} is achieved by the bi-material C-Bm/4–1 strip after 24 h. There is a difference of 0.026 mm^{-1} in curvature to its corresponding reference strip (C-M/4–1), which equals an 82.3 % higher curvature. Furthermore, it is observable that the curvatures of the mono-material reference strips decrease with prolonged water immersion at 70 °C. Between 0.5 h - 24 h, the curvature of the C-M/4–0.3 decreases by 22.3 %. In contrast, the curvature of the bi-material strips is similar for C-Bm/4–1 and C-Bm/4–0.6, while there is an increase in moisture content. Solely, the curvature of C-Bm/4–0.3, which has the highest thickness of hydro active layer, increased by 9.42 % with an increase of water content from 3.27 % to 12.7 %.

Fig. 11 shows the relative expansion of the 90° and 0° layers of the bi-material strips (see Fig. 11a) and mono-material reference strips (see Fig. 11b). Noticeably, the 90° biocomposite layers of the bi-material strips have positive relative expansions that increase with time. The overall highest relative expansion of 9.89 ± 1.70 % is achieved by condition 5 after 24 h. In contrast, the 0° neat PLA layers have shrinkage values that decrease with time. Condition 4 has the highest shrinkage

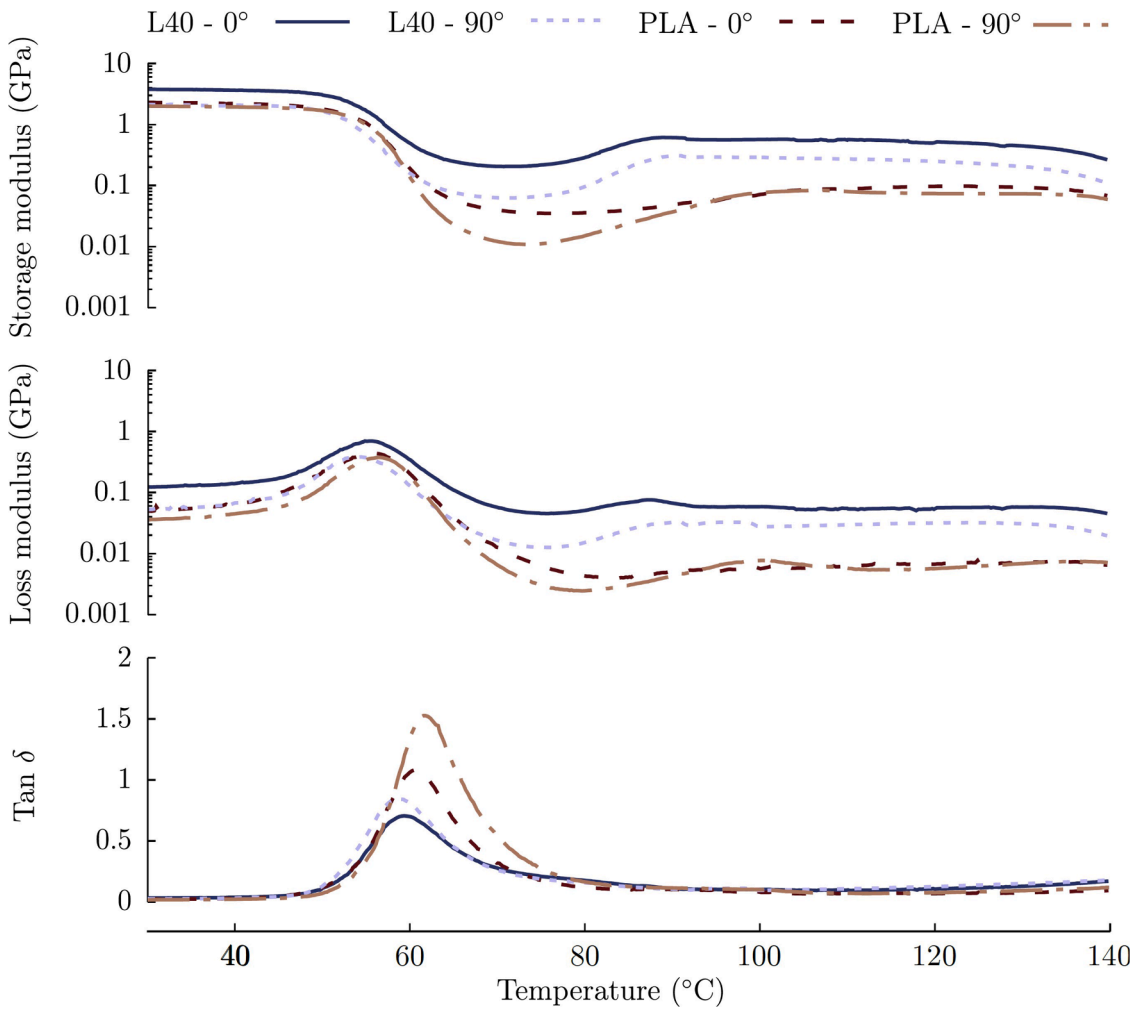

Fig. 5. Effect of 40 wt % lyocell fibres (L40) and raster angle on the storage modulus, loss modulus and tan δ. Solid purple lines and dotted purple lines represent biocomposites printed at raster angles of 0° and 90°, respectively. Samples of neat PLA are shown as dashed brown lines and dashed-dotted brown lines for samples printed at raster angles of 0° and 90°, respectively.

(−22.29 ± 0.51 %) after 30 min and is 1.86 times higher than condition 6. Furthermore, condition 6 decreases by 13.48 % between 30 min - 24 h. The shrinkage behaviour is also observable for the 0° neat PLA layers of the mono-material reference strips. Between 0.5 - 24 h, the shrinkage of reference 4 decreases by 19.15 %. However, in contrast to the bi-material strips, the 90° neat PLA layers also show a small increase of shrinkage values with time. After 30 min, the 90° layers of reference 6 shrank by 1.26 ± 0.69 %, which further increases to 2.97 ± 0.74 % after 24 h.

Fig. 12 compares the curvature resulting from hydromorphic transformation, shape-shifting, and their combined effect in the thickest sample set (4 mm strips). In the hydromorphic condition (Condition 4, Bm/4–1), bi-material strips were immersed in water at 20 °C for 168 h. As expected for such thick samples, the resulting curvature was minimal, measured at 0.0120 ± 0.0002 mm^{-1}. This closely aligns with the curvature predicted by the Timoshenko model for this configuration (0.0100 mm^{-1}). This condition was compared with samples of the same thickness and configuration, condition 5 (C-Bm/4–1), and also compared with mono-material reference samples (C-M/4–1) that were immersed at 70 °C for 24 h. The combination achieves the highest average curvature of 0.057 ± 0.001 mm^{-1}. It is 1.82 times higher than the shape-shifting curvatures and 4.77 times higher than the hydromorphic curvatures.

4. Discussion

The incorporation of 40 wt % lyocell fibres improves the thermophysical and thermomechanical properties.

It has been shown in several studies that adding cellulose fibres can enhance the thermophysical and thermomechanical properties of PLA [10,22,30]. The results of the DSC and DMA show alignment with this. The incorporated lyocell fibres decrease the polymer chain mobility. Thus, the fibres increase the T*g* [31] and reduce the tan *δ*, indicating better thermomechanical stability and less pronounced viscous behaviour [10]. Furthermore, the lyocell fibres act as a nucleating agent for PLA and facilitate cold crystallization, resulting in a decrease of T*cc* and increase in ΔH*cc* *[32]*. The storage modulus increase for the biocomposite in the third region of the DMA corroborates this. It is induced by the formation of crystalline regions during cold crystallization and the resulting restriction of polymer chain mobility [10]. Additionally, the results of the DMA show a dependency of the storage modulus of the biocomposite on the raster angle. The 0° raster angle has the highest storage modulus over the temperature range of 20 - 140 °C, as it induces a favourable fibre orientation that facilitates the stress transfer between printed layers. In contrast, the 90° raster angle creates a fibre orientation with limited stress transfer capacity, leading to a lower storage modulus (as also observed in the neat PLA sample printed at 90°) [33].

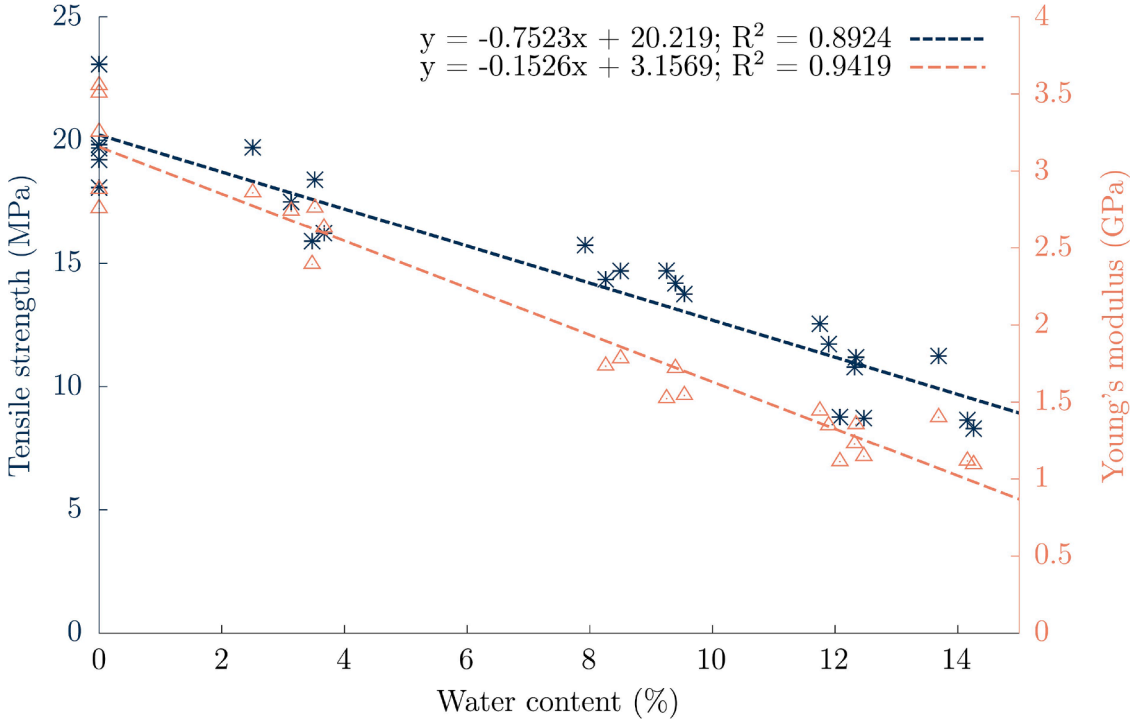

Fig. 6. Effect of water content on the biocomposite's ultimate tensile strength (blue stars and dashed line) and Young's modulus (orange triangles and dash-dotted line) 3D printed using a raster angle of 90° (applied load perpendicular to printing direction).

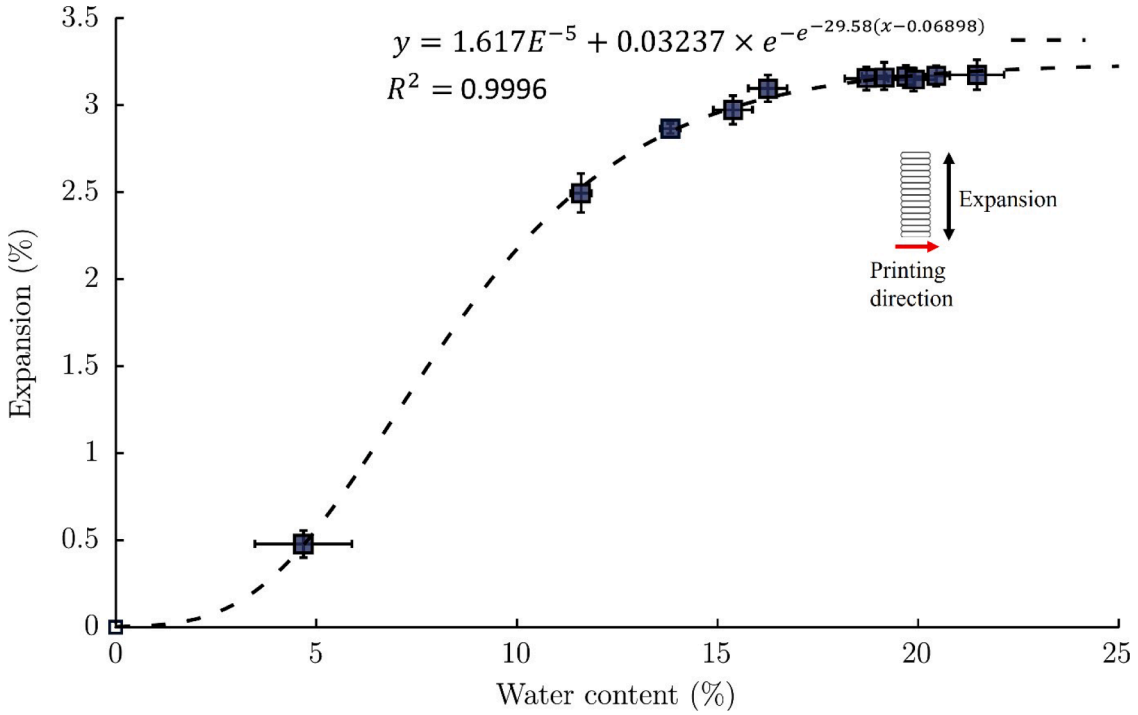

Fig. 7. Effect of water content percentage on the hydroexpansion in the length of the biocomposites (perpendicular to the printing direction). The average hydroexpansion in length follows a sigmoidal curve with an increase in the average water content (triplicates). The error bars represent one standard deviation.

4.1. The water uptake degrades the mechanical properties of the biocomposite

The ingression of water in the biocomposite leads to a decrease in Young's modulus and tensile strength. Upon moisture absorption, the lyocell fibres swell anisotropically in their transverse direction, inducing hoop stresses in the PLA matrix and thus leading to plastic strains and micro-cracks which account for the mechanical degradation. This magnitude of mechanical degradation due to moisture exposure is consistent with findings in the literature. Jiao-Wang et al. (2024) observed that stiffness and yield stress of flax/PLA biocomposites dropped significantly at ~12 % moisture content, although tensile

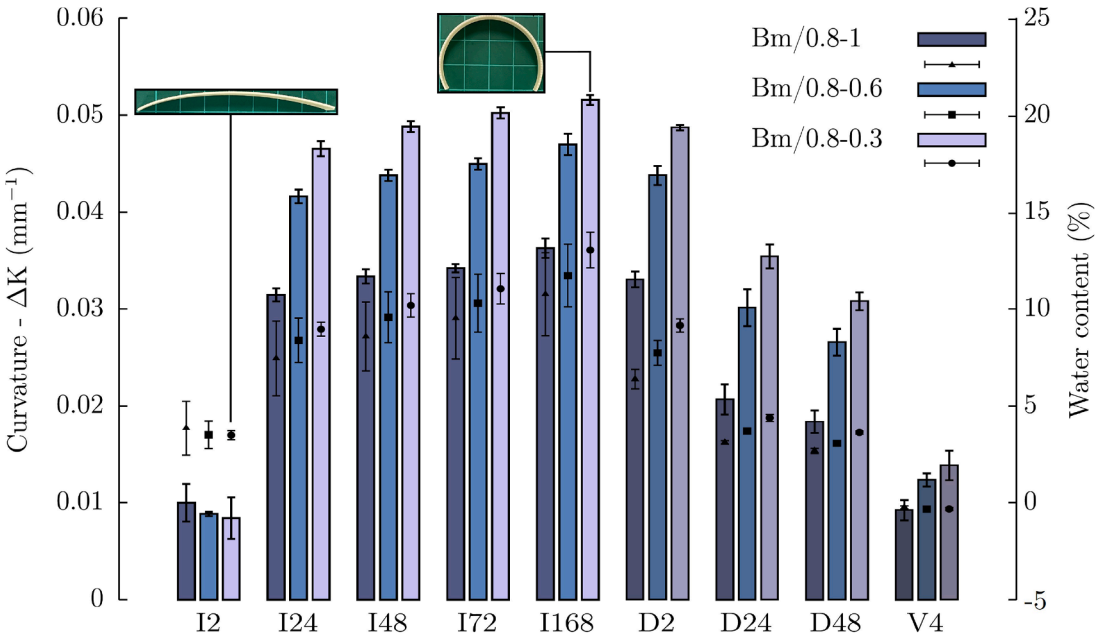

Fig. 8. Average curvature (bars) and water content (symbols) values of conditions with different ratios of passive to active layers (1.0 to 0.33) at different immersion time (abbreviation I + time step (h)) and drying time (abbreviation D + time step (h)) at room conditions. After vacuum drying for 4 h (V4), the moisture contents return to 0 %, while there are remaining curvatures for all conditions. Photos of condition Bm/0.8–0.3 after 2 and 168 h of immersion (grid in background = 1 × 1 cm) are shown on the top.

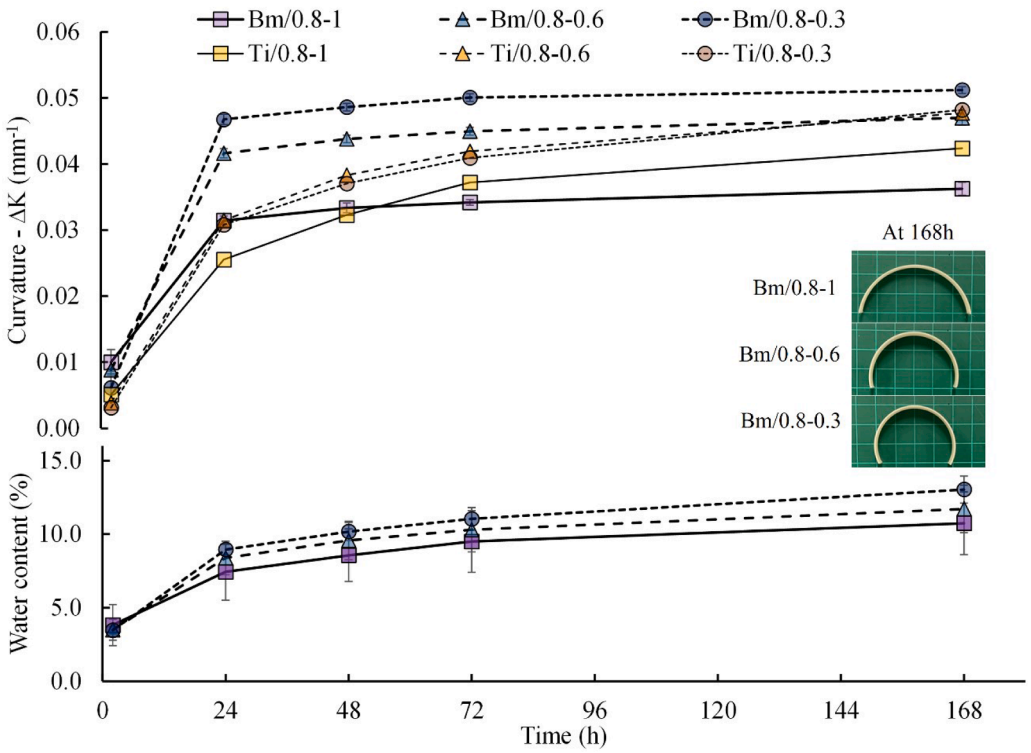

Fig. 9. Experimental curvature and water content for conditions 1 - 3 (Bm/0.8–1; Bm/0.8–0.6; Bm/0.8–0.3) and the corresponding modified Timoshenko equation predicted curvatures (Ti/0.8–1; Ti/0.8–0.6; Ti/0.8–0.3) in comparison.

strength remained more stable in their system, likely due to the woven structure and limited matrix-fibre debonding under their specific test configuration [34]. In contrast, Regazzi et al. (2016) reported a progressive and irreversible decrease in both tensile strength and dynamic elastic modulus in flax-reinforced PLA under hydrothermal aging, with strength losses exceeding 50 % at 50 °C over extended immersion, and noted that the degradation was driven by fibre swelling, microcracking, and matrix hydrolysis [35]. These studies reinforce the critical role of water in disrupting the fibre–matrix interface, reducing stress transfer efficiency, and accelerating physical and chemical aging in biocomposites.

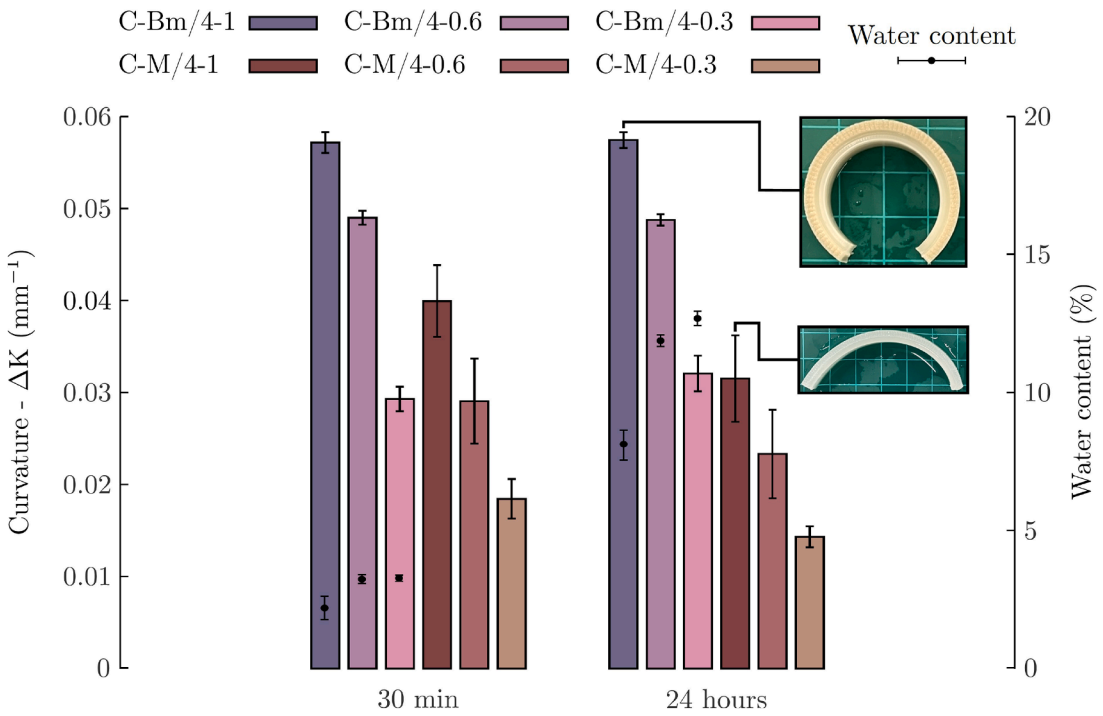

Fig. 10. Average curvatures (bars) and water (symbols) contents of bi-material strips (conditions 5–7) and their corresponding mono-material reference strips (conditions r5-r7) after immersion in water at 70 °C. Also shown are pictures of C-Bm/4–1 and its reference (C-M/4–1) after 24 h of immersion (grid in background = 1 × 1 cm).

4.2. Hydromorphic behaviour and its limited predictability

A handful of studies have covered the hygro-/hydromorphic behaviour of bi-material strips [4,13,36]. For example, Le Duigou and Castro (2017) determined that the optimal range of the passive-to-active layer ratio is between 0.3 and 0.5. The results of hydromorphic strips show alignment with this. Condition 3 (Bm/0.8–0.03) achieved the highest curvature values with a ratio $m = 0.33$. Tomec et al. (2021) reported that with an increase in the active layer content of the bi-material strip, the reactiveness decreases, and it takes longer for the moisture content to reach a state of equilibrium. This phenomenon is observable after 2 h of immersion in water, where condition 1 (Bm/0.8–1) has the greatest curvature with a passive/active layers ratio of 1, and condition 3 (Bm/0.8–0.3) has the lowest curvature with a ratio of 0.33. The limited reversibility can be related to the same mechanism that induces the degradation of the mechanical properties of the biocomposite [4]. Greater moisture contents cause higher hygroscopic stresses, resulting in greater irreversible plastic strains and, thus, lesser reversibility.

The modified Timoshenko equation predicts curvature only moderately well; it tends to underestimate curvature, although accuracy improves when ratio $m = 1$. Le Duigou and Castro (2017) refer transverse stresses to this, as these may have appeared due to the Poisson's coefficient mismatch and anisotropic properties. Consequently, for more precise predictions, further adjustments to the equation are required. To improve predictive accuracy, three correction factors could be added to the modified Timoshenko equation: (i) a moisture-gradient factor that scales curvature with the depth-dependent swelling of the active layer, (ii) a transverse-stress factor that accounts for Poisson mismatch and the resulting in-plane compression, and (iii) a shear-lag factor to capture through-thickness shear dependent on the passive-to-active thickness ratio.

4.3. The combination of the shape-shifting and hydromorphic effects induces greater curvature and faster shape transformation

The results demonstrate that combining hydromorphic and shape-shifting effects leads to a greater curvature change within a shorter exposure time and offers improved dimensional stability during prolonged immersion, compared to each mechanism applied independently. This increased curvature arises from the differential response between the biocomposite and neat PLA layers [37], where the biocomposite layer tends to expand while the PLA layer contracts. Importantly, the bi-material configuration contributes to maintaining the induced shape over time, unlike the neat PLA, which exhibits progressive deformation when immersed. When the fibres in the biocomposites layer absorb moisture, they swell anisotropically in their transverse direction [1]. Thus, expansion occurs mainly perpendicular to the fibre orientation. By 3D printing the biocomposite in a 90° raster angle, the lyocell fibres were aligned with that angle through shear forces[22]. This predominant fibre orientation caused the biocomposite layer to expand parallel to the length of the bi-material strip. Additionally, the neat PLA layer shrinks parallel to the 0° raster angle and thus parallel to the length of the bi-material strip. During 3D printing, shear forces within the nozzle align the polymer chains in the printing direction, while fan cooling locks them in this stretched, low-entropy state. While reheating, the built-in strain is released, as the polymer chains retain their high entropy equilibrium state, which induces the shrinkage [19,38]. Thus, the hydroexpansion of the biocomposite combined with the shrinkage of the neat PLA increases the size difference between the layers and induces greater curvatures. Furthermore, the enhanced stability of the curvature with prolonged immersion at 70 °C is possibly induced by the improved thermomechanical properties and the hygro-expansion of the biocomposite.

It was observed that the curvature of the PLA-only reference strips decreased with prolonged immersion time in water at 70 °C. The reason for the decrease in curvature is the shrinkage of the 90° neat PLA layer and the expansion of the 0° neat PLA layer between 30 min – 24 h. Essentially, what happens is an inverse behaviour compared to that of

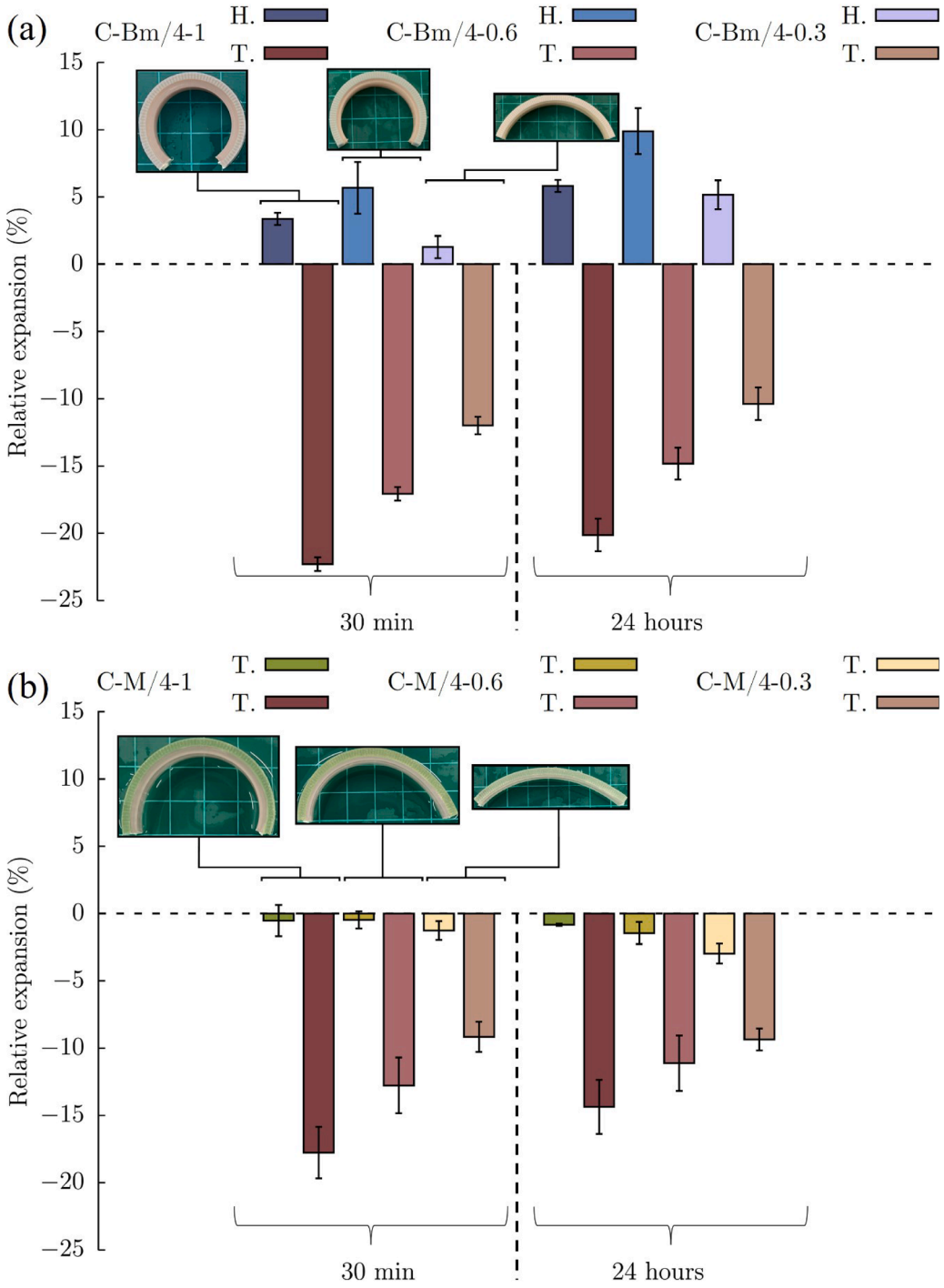

Fig. 11. Average relative expansion (triplicates) of the passive and active layers of the bi-material (a) and mono-material reference strips (b). It is visible that the 90° bi-material strip layers (blue bars, 4 - 6 from left to right) have positive expansions that increase with time, while the 0° layers (red bars) show shrinkage that decrease with time. In contrast, the 90° (green bars, r4 - r6 from left to right) and 0° (red bars) layers both show shrinkage.

the bi-material strip, resulting in a decrease of the size difference between those layers and, thus, a decrease in curvature [37]. After 24 h, a reduction in transparency was observed, indicating the onset of crystallization (see Figure S3) [39]. Although the crystallization temperature for this grade of PLA is approximately 120 °C, partial ordering of the amorphous regions can begin even at 70 °C, which is close to its glass transition temperature (Tg), due to increased chain mobility, albeit at a significantly slower rate [40]. Consequently, both expansion and shrinkage over time can be attributed to the anisotropic nature of PLA crystallization, influenced by the printing orientation and resulting alignment of polymer chains.

Since the hydroexpansion of the biocomposite layer and the expansion of the neat PLA layer occur simultaneously between 0.5 and 24 h of immersion, their effects appear to counterbalance each other. Therefore, the size difference between the layers remains the same, and thus the curvature, too. As for this, condition 5–6 curvatures are constant with time. The slight increase in the curvature of condition 7 might be because of the greater amount of active layer and, thus, a delayed reactiveness. Here, the hydroexpansion exceeded the expansion of the neat PLA with time, resulting in a slightly greater size difference

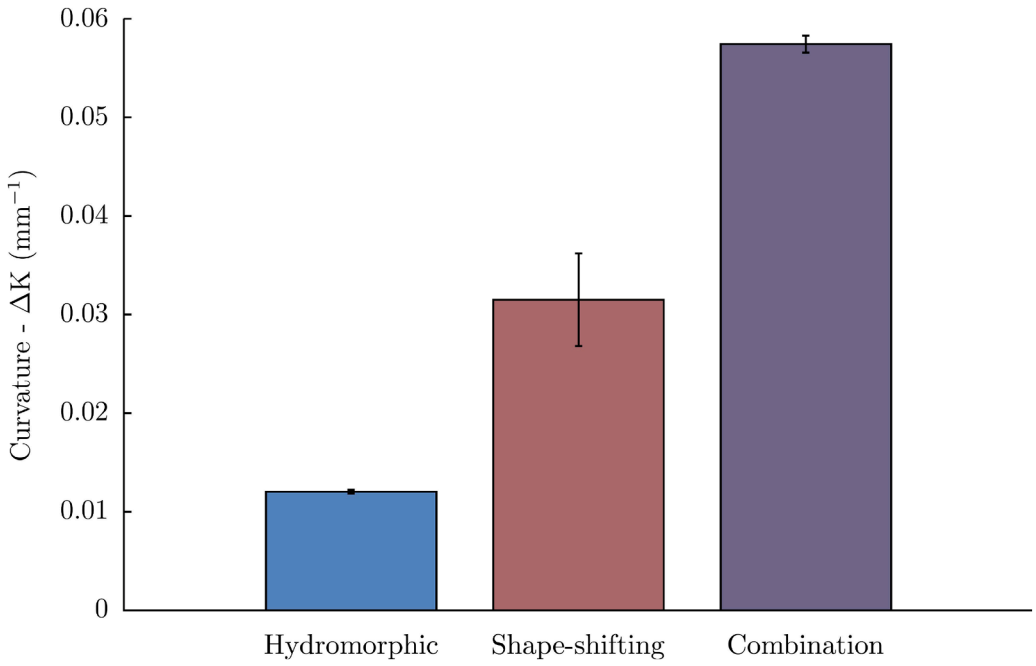

Fig. 12. Average curvatures (triplicates) of sample Bm/4–1 for the isolated hydromorphic, reference C-M/4–1 for shape-shifting-effect and C-Bm/4–1 for their combination.

between the layers.

In summary, the biocomposite containing 40 wt % of lyocell exhibits favourable thermomechanical and thermophysical properties, along with effective hydroexpansion behaviour, making it well suited for use in bi-material strips. By combining hydromorphic and shape shifting effects, a greater degree of shape transformation was achieved, along with more stable curvature during extended exposure to hot water, compared to the use of either effect alone. Despite these advantages, the approach has limitations regarding reversibility. While hydromorphic shape change is inherently reversible, the shape shifting behaviour of PLA cannot be reversed simply by lowering the temperature. To restore the material to its original flat configuration, it is necessary to apply external force at a temperature above the glass transition point, followed by cooling below that temperature. Although reversibility was not the primary focus of this study, it is expected that if the material undergoes a second thermal cycle above the glass transition point—after flattening and cooling—it would return quickly to the bent or curved shape due to the shape memory properties of PLA. Therefore, this combined method may serve as a reliable programming step for future applications that seek to harness the reversible response enabled by shape memory behaviour.

5. Conclusion

In this study, we demonstrated that the combination of the hydromorphic and shape-shifting effects leads to increased curvature and faster response in 4D printing applications. By promoting a predominant fibre orientation in the biocomposite during printing, the anisotropic swelling of lyocell fibres was leveraged to fabricate bi-material hydromorphic structures. Additionally, by stretching and constraining PLA polymer chains through the printing process, the thermal shrinkage of PLA, triggered at temperatures higher than the glass transition temperature, was used to implement the shape-shifting effect into the structure. The hydroexpansion of the biocomposite layer and thermal shrinkage of the PLA layer in the bi-material strip produced a larger dimensional mismatch between the two, resulting in greater curvature change and faster shape transformation when subjected to water and heat. This approach offers potential for smart systems where controlled shape change in thick structures is essential, with prospective applications in load-bearing components such as furniture and architectural elements. Moreover, it may serve as an effective programming step for activating shape memory behaviour in future responsive material systems.

Declaration of generative AI and AI-assisted technologies in the writing process

During the preparation of this work the author(s) used generative AI writing tool from ChatGPT (OpenAI) to improve clarity and remove grammar mistakes of our original writing from some sections of this manuscript. After using this tool/service, the authors reviewed and edited the content as needed and take full responsibility for the content of the published article.

CRediT authorship contribution statement

Phil Aron Bachmann: Writing – original draft, Methodology, Investigation, Formal analysis. **Kim Pickering:** Writing – review & editing, Funding acquisition. **Christian Gauss:** Writing – review & editing, Supervision, Formal analysis, Conceptualization.

Declaration of competing interest

The authors declare that they have no known competing financial interests or personal relationships that could have appeared to influence the work reported in this paper.

Acknowledgements

The authors would like to thank the Ministry of Business, Innovation and Employment (MBIE) New Zealand Endeavour Fund, for funding through the project Āmiomio Aotearoa – A circular Economy for the wellbeing of New Zealand (UOWX2004) and the National Science Challenge spearhead project “Additive manufacturing and 3D and/or 4D printing of biocomposites” [grant 2019-S5-CRS].

Supplementary materials

Supplementary material associated with this article can be found, in the online version, at doi:10.1016/j.jcomc.2025.100632.

Data availability

Data will be made available on request.

References

[1] E.K. Gamstedt, Moisture induced softening and swelling of natural cellulose fibres in composite applications, in: IOP Conf Ser Mater Sci Eng 139, Institute of Physics Publishing, 2016, https://doi.org/10.1088/1757-899X/139/1/012003.

[2] Stamboulis A., Baillie C.A., Garkhail S.K., Van Melick H.G.H., Peijs T. Environmental Durability of Flax Fibres and their Composites based on Polypropylene Matrix. vol. 7. 2000.

[3] C. Dawson, J.F .V.. Vincent, A. Rocca, How pine cones open, Scient. Corresp. Nat. 390 (1997) 668. –668.

[4] C. Gauss, K. Pickering, M. Barbier, T. Miller, Additive manufacturing of hygromorphic structures using regenerated cellulose/PLA biocomposites, Mater. Today. Proc. (2023), https://doi.org/10.1016/j.matpr.2023.04.227.

[5] A. Le Duigou, M. Castro, R. Bevan, N. Martin, 3D printing of wood fibre biocomposites: from mechanical to actuation functionality, Mater. Des. 96 (2016) 106–114, https://doi.org/10.1016/j.matdes.2016.02.018.

[6] C. De Kergariou, A. Le Duigou, A. Perriman, F. Scarpa, Design space and manufacturing of programmable 4D printed continuous flax fibre polylactic acid composite hygromorphs, Mater. Des. 225 (2023), https://doi.org/10.1016/j.matdes.2022.111472.

[7] A. Sydney Gladman, E.A. Matsumoto, R.G. Nuzzo, L. Mahadevan, J.A Lewis, Biomimetic 4D printing- Supporting Information, Nat. Mater. 15 (2016) 413–418, https://doi.org/10.1038/nmat4544.

[8] D. Klemm, B. Heublein, H.P. Fink, A. Bohn, Cellulose: fascinating biopolymer and sustainable raw material, Angew. Chem. - Internat. Ed. 44 (2005) 3358–3393, https://doi.org/10.1002/anie.200460587.

[9] H. Santamala, R. Livingston, H. Sixta, M. Hummel, M. Skrifvars, O. Saarela, Advantages of regenerated cellulose fibres as compared to flax fibres in the processability and mechanical performance of thermoset composites, Compos. Part A Appl. Sci. Manuf. 84 (2016) 377–385, https://doi.org/10.1016/j.compositesa.2016.02.011.

[10] C. Gauss, K.L. Pickering, J. Tshuma, J. McDonald-Wharry, Production and assessment of poly(Lactic Acid) matrix composites reinforced with regenerated cellulose fibres for fused deposition modelling, Polymers (Basel) 14 (2022) 3991, https://doi.org/10.3390/polym14193991.

[11] S. Okubayashi, U.J. Griesser, T. Bechtold, Moisture sorption/desorption behavior of various manmade cellulosic fibers, J. Appl. Polym. Sci. 97 (2005) 1621–1625, https://doi.org/10.1002/app.21871.

[12] Q. Ge, A.H. Sakhaei, H. Lee, C.K. Dunn, N.X. Fang, M.L. Dunn, Multimaterial 4D printing with tailorable shape memory polymers, Sci. Rep. 6 (2016) 1–11, https://doi.org/10.1038/srep31110.

[13] D.K. Tomec, A. Straže, A. Haider, M. Kariž, Hygromorphic response dynamics of 3d-printedwood-PLA composite bilayer actuators, Polymers (Basel) 13 (2021), https://doi.org/10.3390/polym13193209.

[14] S. Tibbits, 4D printing: multi-material shape change, Architect. Des. 84 (2014) 116–121, https://doi.org/10.1002/ad.1710.

[15] Q. Zhang, D. Yan, K. Zhang, G. Hu, Pattern Transformation of heat-shrinkable polymer by three-dimensional (3D) printing technique, Sci. Rep. 5 (2015), https://doi.org/10.1038/srep08936.

[16] H. Yang, W.R. Leow, T. Wang, J. Wang, J. Yu, K. He, et al., 3D printed photoresponsive devices based on shape memory composites, Adv. Mater. 29 (2017) 1–7, https://doi.org/10.1002/adma.201701627.

[17] M. Nadgorny, Z. Xiao, C. Chen, L.A Connal, Three-dimensional printing of pH-responsive and functional polymers on an affordable desktop printer, ACS Appl. Mater. Interf. 8 (2016) 28946–28954, https://doi.org/10.1021/acsami.6b07388.

[18] Q. Zhao, H.J. Qi, T. Xie, Recent progress in shape memory polymer: new behavior, enabling materials, and mechanistic understanding, Prog Polym Sci 49–50 (2015) 79–120, https://doi.org/10.1016/j.progpolymsci.2015.04.001.

[19] E. Hornbogen, Comparison of shape memory metals and polymers, Adv. Eng. Mater. 8 (2006) 101–106, https://doi.org/10.1002/adem.200500193.

[20] F. Wang, F. Luo, Y. Huang, X. Cao, C. Yuan, 4D printing via multispeed fused deposition modeling, Adv. Mater. Technol. 8 (2023) 1–8, https://doi.org/10.1002/admt.202201383.

[21] N. Graupner, S. Schmidt, C. Gauss, J. Müssig, Making positive use of the fibrillation of lyocell fibres in composite materials, Compos. Part C: Open Access 11 (2023), https://doi.org/10.1016/j.jcomc.2023.100359.

[22] C. Gauss, K.L. Pickering, N. Graupner, J. Müssig, 3D-printed polylactide composites reinforced with short lyocell fibres – Enhanced mechanical properties based on bio-inspired fibre fibrillation and post-print annealing, Addit. Manuf. 77 (2023), https://doi.org/10.1016/j.addma.2023.103806.

[23] S. Pilla, S. Gong, E. O'Neill, R.M. Rowell, A.M Krzysik, Polylactide-pine wood flour composites, Polym. Eng. Sci. 48 (2008) 578–587, https://doi.org/10.1002/pen.20971.

[24] A. Holstov, B. Bridgens, G. Farmer, Hygromorphic materials for sustainable responsive architecture, Constr. Build. Mater. 98 (2015) 570–582, https://doi.org/10.1016/j.conbuildmat.2015.08.136.

[25] A. Le Duigou, V. Keryvin, J. Beaugrand, M. Pernes, F. Scarpa, M. Castro, Humidity responsive actuation of bioinspired hygromorph biocomposites (HBC) for adaptive structures, Compos. Part A Appl. Sci. Manuf. 116 (2019) 36–45, https://doi.org/10.1016/j.compositesa.2018.10.018.

[26] J.O. Akindoyo, K. Pickering, M.D. Beg, M. Mucalo, Combined digestion and bleaching of New Zealand flax /harakeke fibre and its effects on the mechanical, thermal, and dynamic mechanical properties of poly(lactic) acid matrix composites, Compos. Part A Appl. Sci. Manuf. 164 (2023), https://doi.org/10.1016/j.compositesa.2022.107326.

[27] F.X. Espinach, S. Boufi, M. Delgado-Aguilar, F. Julián, P. Mutjé, J.A. Méndez, Composites from poly(lactic acid) and bleached chemical fibres: thermal properties, Compos. B Eng. 134 (2018) 169–176, https://doi.org/10.1016/j.compositesb.2017.09.055.

[28] L. Incarnato, M.R. Nobile, P. Scarfato, Development of PLA/Microcellulose Biocomposite filaments for 3D printing, Macromol. Symp. 405 (2022), https://doi.org/10.1002/masy.202100250.

[29] M.D.H. Beg, K.L. Pickering, C. Gauss, The effects of alkaline digestion, bleaching and ultrasonication treatment of fibre on 3D printed harakeke fibre reinforced polylactic acid composites, Compos. Part A Appl. Sci. Manuf. 166 (2023) 107384, https://doi.org/10.1016/j.compositesa.2022.107384.

[30] M. Jonoobi, J. Harun, A.P. Mathew, K. Oksman, Mechanical properties of cellulose nanofiber (CNF) reinforced polylactic acid (PLA) prepared by twin screw extrusion, Compos. Sci. Technol. 70 (2010) 1742–1747, https://doi.org/10.1016/j.compscitech.2010.07.005.

[31] T. Yu, N. Jiang, Y. Li, Study on short ramie fiber/poly(lactic acid) composites compatibilized by maleic anhydride, Compos. Part A Appl. Sci. Manuf. 64 (2014) 139–146, https://doi.org/10.1016/j.compositesa.2014.05.008.

[32] B.H. Lee, H.S. Kim, S. Lee, H.J. Kim, J.R. Dorgan, Bio-composites of kenaf fibers in polylactide: role of improved interfacial adhesion in the carding process, Compos. Sci. Technol. 69 (2009) 2573–2579, https://doi.org/10.1016/j.compscitech.2009.07.015.

[33] I.M. Alarifi, Investigation of the dynamic mechanical analysis and mechanical response of 3D printed nylon carbon fiber composites with different build orientation, Polym. Compos. 43 (2022) 5353–5363, https://doi.org/10.1002/pc.26838.

[34] L. Jiao-Wang, S. Charca, J. Abenojar, M.A. Martínez, C. Santiuste, Moisture effect on tensile and low-velocity impact tests of flax fabric-reinforced PLA biocomposite, Polym. Compos. 45 (2024) 11816–11828, https://doi.org/10.1002/pc.28601.

[35] A. Regazzi, S. Corn, P. Ienny, J.C. Bénézet, A. Bergeret, Reversible and irreversible changes in physical and mechanical properties of biocomposites during hydrothermal aging, Ind. Crops .Prod. 84 (2016) 358–365, https://doi.org/10.1016/j.indcrop.2016.01.052.

[36] A. Le Duigou, M. Castro, Hygromorph BioComposites: effect of fibre content and interfacial strength on the actuation performances, Ind. Crops. Prod. 99 (2017) 142–149, https://doi.org/10.1016/j.indcrop.2017.02.004.

[37] Y.S. Alshebly, M. Nafea, Effects of printing parameters on 4D-printed PLA actuators, Smart. Mater. Struct. 32 (2023), https://doi.org/10.1088/1361-665X/acd504.

[38] Q. Zhang, D. Yan, K. Zhang, G. Hu, Pattern Transformation of heat-shrinkable polymer by three-dimensional (3D) printing technique, Sci. Rep. 5 (2015), https://doi.org/10.1038/srep08936.

[39] Saitou K.-.I., Yamaguchi M. Transparent poly(lactic acid) film crystallized by annealing beyond glass transition temperature 2071. https://doi.org/10.1007/s10965-020-02071-y/Published.

[40] M.L. Di Lorenzo, Crystallization behavior of poly(l-lactic acid), Eur. Polym. J. 41 (2005) 569–575, https://doi.org/10.1016/j.eurpolymj.2004.10.020.